Environmental Control of Wind Response to Sea Surface Temperature Patterns in Reanalysis Dataset

Fabien Desbiolles, Agostino N. Meroni, Lionel Renault, Laudia Pasquero

SPECIAL
Climate Implications of Air-Sea Interaction
COLLECTION

Environmental Control of Wind Response to Sea Surface Temperature Patterns in Reanalysis Dataset

FABIEN DESBIOLLES,[a,b] AGOSTINO N. MERONI,[a] LIONEL RENAULT,[c] AND CLAUDIA PASQUERO[a,d]

[a] *Department of Earth and Environmental Sciences, Università di Milano–Bicocca, Milan, Italy*
[b] *CIMA Research Foundation, Savona, Italy*
[c] *LEGOS, University of Toulouse, IRD, CNRS, CNES, UPS, Toulouse, France*
[d] *Istituto di Scienze dell'Atmosfera e del Clima, Consiglio Nazionale delle Ricerche, Turin, Italy*

(Manuscript received 18 May 2022, in final form 13 February 2023, accepted 17 February 2023)

ABSTRACT: Sea surface temperature (SST) is characterized by abundant warm and cold structures that influence the overlying atmospheric boundary layer dynamics through two different mechanisms. First, turbulence and large eddies in the lower troposphere are affected by atmospheric stability, which can be modified by local SST, resulting in enhanced vertical mixing and larger surface winds over warmer waters. Second, the thermodynamic adjustment of air density to the underlying SST structures and the subsequent changes in atmospheric pressure drive secondary circulations. This paper aims to disentangle the effects of these processes and explore the environmental conditions that favor them. Two main environmental variables are considered: the large-scale air–sea temperature difference (proxy for stability) and wind speed. Using 5 years of daily reanalyses data, we investigate the 10-m wind response to SST structures. Based on linear regression between wind divergence and SST derivatives, we show that both mechanisms operate over a large spectrum of conditions. Ten-meter wind divergence is strongly impacted by the local SST via its effect on vertical mixing for midwind regimes in slightly unstable to near-neutral conditions, whereas the secondary circulation is important in two distinct regimes: low wind speed with a slightly unstable air column and high background wind speed with a very unstable air column. The first regime is explained by the prolonged Lagrangian time that the air parcel stays over an SST structure while the second one is related to strong heat fluxes at the air–sea interface, which greatly modify the marine atmospheric boundary layer properties. Location and frequency of the environmentally favorable conditions are discussed, as well as the response in low-cloud cover and rainfall.

SIGNIFICANCE STATEMENT: The main objective of this study is to explore the wind response to thermal structures at the sea surface under different environmental conditions using the latest atmospheric reanalysis. Recent literature suggests that fine-scale air–sea interactions affect a large spectrum of atmospheric dynamics, from seasonal to weather-type regimes. It is thus important to characterize the atmospheric response to ocean surface variability. Our findings describe the environmental conditions for which the two main physical processes through which the atmosphere responds to sea surface temperature structures are active the most and can guide the development of high-resolution observing missions and campaigns in specific geographical locations and seasons to retrieve data that can be used to improve parameterization in models.

KEYWORDS: Air-sea interaction; Reanalysis data; Marine boundary layer; Precipitation

1. Introduction

Thermal properties of the oceanic surface layer are of paramount importance for tropospheric dynamics, as they affect air temperature and moisture content. Sea surface temperature (SST) mesoscale structures, $\mathcal{O}(10-500)$ km, such as long-lived eddies, transient tropical cyclone cold wakes and fronts, can generate spatial variability in the lower troposphere and eventually affect atmospheric jets, cloudiness, and precipitation (e.g., Frenger et al. 2013; Minobe et al. 2008; Pasquero et al. 2021; Desbiolles et al. 2021). The atmospheric response to thermal patterns also includes the generation of

Denotes content that is immediately available upon publication as open access.

Supplemental information related to this paper is available at the Journals Online website: https://doi.org/10.1175/JCLI-D-22-0373.s1.

Corresponding author: Fabien Desbiolles, fabien.desbiolles@unimib.it

DOI: 10.1175/JCLI-D-22-0373.1

small-scale variability at the interface such as wind stress curl and divergence anomalies (Chelton et al. 2004) and turbulent heat flux anomalies (Bishop et al. 2020) that feed back onto the surface ocean properties [e.g., review of Small et al. (2008) and the references therein].

Two main mechanisms have been identified to characterize the atmospheric dynamical response to mesoscale SST anomalies: the downward momentum mixing (DMM) mechanism, notably introduced by Hayes et al. (1989), and the pressure adjustment (PA) mechanism, highlighted by Lindzen and Nigam (1987).

For the DMM, the vertical extension of the turbulent eddies in the marine atmospheric boundary layer (MABL) depends on the stratification, resulting in a vertical turbulent mixing of momentum that is a function of the air column stability. Indeed, a wind blowing from cold to warm (warm to cold) SST favors the increase (decrease) of the air potential temperature and humidity and weakens (strengthens) the vertical wind shear, enhancing (inhibiting) the coupling with the winds aloft. For this reason, surface winds over the cold flank of an SST front tend to be weaker than on the warm flank, where the coupling with the winds aloft is stronger (Wallace et al. 1989). At monthly time scales and at the upper bound of the oceanic mesoscales (i.e., ~500 km), a linear relationship emerges between wind and SST perturbations (i.e., high-pass filtered) and between appropriate derivative fields (downwind SST gradient and wind and/or wind stress divergence; O'Neill et al. 2003; Chelton et al. 2004, 2007; O'Neill et al. 2005; Desbiolles et al. 2014). Samelson et al. (2006) early argued with an analytical model the wind response to an ocean front is asymmetric, with a more important DMM response for the cold-to-warm transitions.

For the PA mechanism, the air parcel thermodynamically adjusts to the underlying SST affecting air density and pressure (Lindzen and Nigam 1987). This drives pressure gradients on geopotential surfaces that generate secondary circulations (Wai and Stage 1989). Initially proposed in a context of tropical dynamics, PA causes wind divergence in the MABL due to surface atmospheric pressure anomalies forced by temperature patterns (Lindzen and Nigam 1987). It ensues a linear relationship between wind divergence and the Laplacian of SST (e.g., Lambaerts et al. 2013; Takatama and Schneider 2017). This pressure adjustment mechanism has been successfully used to describe the response of the MABL properties to SST structures in different contexts and dynamical backgrounds; modeling works analyzed it in realistic (e.g., over western boundary currents, WBCs; Minobe et al. 2008) and in idealized configurations (Lambaerts et al. 2013). Other works, such as Li and Carbone (2012) and Skyllingstad et al. (2019), show that in the tropical ocean the mesoscale SST structures can trigger atmospheric convection through the PA mechanism.

The above two mechanisms, DMM and PA, strongly involve turbulent heat fluxes (THFs, both latent and sensible) variability, notably the change in sensible and latent heat flux when air blows over an SST structure, modulating near-surface stability (Businger and Shaw 1984; Hayes et al. 1989). It has recently been shown that air–sea turbulent heat flux anomalies are a sink of energy for the ocean at mesoscales (Bishop et al. 2020), modulating ocean transient structures and SST gradients. A full feedback loop is then present and both fluids react to each other. Due to the nonlinear nature of the THFs with the wind speed and the air-column stability, particular care is needed to investigate the thermal feedbacks in different weather conditions. For example, O'Neill et al. (2012) discuss the sensitivity of DMM to wind speed in a climatological sense. They notably argue that, over WBCs, the winter season exhibits a stronger coupling due to the greater large-scale wind stress. More recently, Schneider (2020) highlighted that the wind response depends on the background wind speed, the spatial scale of the SST structure and the Rossby number. In his work, he shows that DMM- and PA-mediated wind response can be disentangled by estimating response and transfer functions from satellite data.

Recent studies have shown that the MABL responds to SST structures by developing the secondary circulation associated with the PA mechanism both at mesoscales and submesoscales, with notable asymmetries depending on the sign of the SST anomaly (Lambaerts et al. 2013). They argue that positive SST anomalies induce a stronger change in the stability of the MABL compared to negative ones of the same order of magnitude. The former leads to an enhancement of dry convection that reinforces PA. On the contrary, negative SST anomalies stimulate divergence in the MABL that inhibits the PA response (Lambaerts et al. 2013).

Some studies show that the relative importance of DMM and PA depends on cross-frontal wind velocity with respect to the front size (Spall 2007; Small et al. 2008; Foussard et al. 2019) and on the boundary layer stability (Foussard et al. 2019). The time scale of these processes are discussed in the recent literature and it has been shown that the wind is responsive at short time scale (daily or subdaily) (Lambaerts et al. 2013; Meroni et al. 2018) for a wide range of weather conditions, from weak and steady background wind (Lindzen and Nigam 1987) to intense storms associated with atmospheric frontal dynamics (Meroni et al. 2020).

The impact of air-column stability and background wind speed in shaping the MABL thermodynamic properties has been considered since the pioneering work on the physical description of the boundary layer by Smith et al. (1914). The recent development of coupled models fostered a better understanding of the thermal feedback processes in state-of-the-art models, allowing finer descriptions and acknowledging the limits of turbulence closure schemes. This paper aims to determine the favorable environmental conditions over which DMM and PA are emphasized and susceptible to most efficiently drive converging and diverging cells in the MABL. Using ERA5 data (Hersbach et al. 2020), the sensitivity of the two thermal feedback mechanisms to environmental atmospheric conditions over the global ocean is discussed. Section 2 introduces the data and different metrics used, and section 3 shows the control of the background air–sea temperature difference and wind speed on DMM and PA. Section 4 discusses the geographical distribution and the frequency of the favorable environmental conditions for DMM and PA superimposed with ocean structures. Conclusions are drawn in section 5.

2. Data and methods

This study uses ERA5 (Hersbach et al. 2020), which is the reanalysis dataset with the finest spatial resolution available (roughly 0.25° globally), obtained with a four-dimensional variational data assimilation approach within the Integrated Forecast System (IFS). More specifically, we use daily mean values of SST, 2-m air temperature, 10-m horizontal wind, low-cloud cover, and total rainfall. The daily means correspond to the average of the hourly outputs downloaded from the Copernicus sever (https://cds.climate.copernicus.eu/cdsapp#!/dataset/reanalysis-era5-single-levels?tab=overview). The period of investigation is 5 years long (2007–11). It was verified that a shorter period (1 year only) does not significantly modify the results of the study, and a longer investigation period was avoided due to the large amount of data to be analyzed (see Fig. S1 in the online supplemental material).

To better isolate mesoscale SST effects on wind variability, a coastal mask is applied on each field. It covers a strip of about 50 km off the coast over which atmospheric dynamics is also driven by several different processes such as land–sea breeze and orographic effects [e.g., Drobinski et al. (2018); Buzzi et al. (2020); Desbiolles et al. (2014); Renault et al. (2016) over eastern boundary upwelling systems, EBUSs]. A geographical boundary has been set at 60° for both hemispheres to restrain the analyses on the ice-free ocean.

A spatial filter is applied to both wind and SST to define the large-scale components which are mainly characterized by a dynamics in which the atmosphere forces the ocean (Chelton and Xie 2010; Gentemann et al. 2020). To this purpose, a Lanczos filter is applied, with a 2D half-power cutoff wavelength of 10° (~1000 km in longitude and latitude). Figure 1 shows the spatial horizontal power spectra of the original (solid lines), low-pass filtered (dashed lines) and the residual (dotted lines) SST (blue) and wind speed (black). As expected, results show that spatial scales on the order of several hundred kilometers, which roughly correspond to those of the upper mesoscale processes, are removed in the low-pass filtered field (dashed lines, hereafter referred to as background field) and kept in the anomaly fields, computed as the difference between the original and the background fields, that will be analyzed in the following. A simple sensitivity analysis to the scale of the filter has been performed. Using a filter cutoff wavelength of 5°, the results are very similar to those presented here. With a filter cutoff wavelength reduced to 2°, the results change: in this case the residual SST field is essentially white noise, because the effective resolution of ERA5 is about 200 km as highlighted in Fig. 1 (considering the effective resolution to be a factor from 5 to 10 larger than the grid spacing, as commonly done with numerical models). The reader is referred to Fig. S2 of the supplemental material.

The background components of the horizontal wind at 10 m are used to determine the intensity and the direction of the background wind [denoted with $\mathbf{U} = (U, V)$, with its eastward and northward components, respectively]. We then define a local Cartesian frame of reference $\{\hat{r}, \hat{s}\}$ based on this large-scale wind vector, with $\hat{r}$ being the along-wind direction and $\hat{s}$ the across-wind direction (positive at 90° counterclockwise with respect to $\hat{r}$), as in Meroni et al. (2022). This local geometrical transformation is useful since the DMM and PA

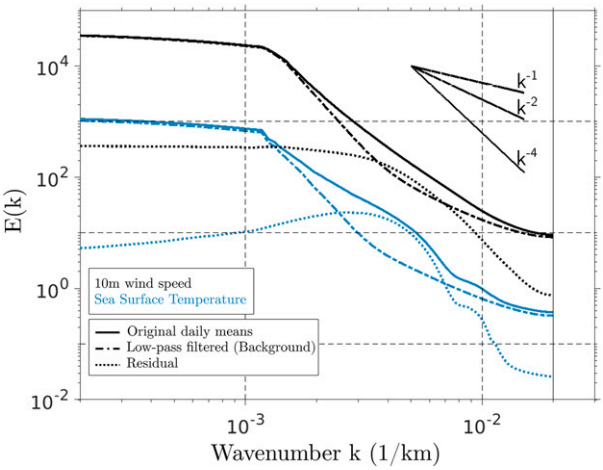

FIG. 1. Time-average wavenumber spectra of SST (blue) and wind speed (black) of the original daily means (solid lines) data, the low-pass filtered fields (dashed lines, defined as background variables in the text), and the residual field (dotted lines). The theoretical slopes k^{-1}, k^{-2}, and k^{-4} are drawn for comparison. Spectra are computed onto the original grid and over the most extended ocean domain (the entire Pacific Ocean). Units of the power spectra are $m^2\ s^{-2}$ km and K^2 km for the wind speed and the SST fields, respectively.

signatures are mostly visible when an air parcel blows across and along an SST front, respectively. A similar approach is used in Schneider (2020) to characterize and separate both DMM and PA responses in the spectral domain. The details of the definition of the considered Cartesian frame and the detailed calculation of the gradient, the divergence and the Laplacian operators are given in appendix.

The metrics used to highlight the processes at work are built in this new Cartesian frame of reference. The usual metrics definitions highlighting thermal feedback mechanisms consider relationships between wind divergence and along-wind SST gradient for DMM and wind divergence and SST Laplacian for PA (e.g., Chelton et al. 2001; Lambaerts et al. 2013; Small et al. 2008; Meroni et al. 2018; Takatama and Schneider 2017). Following Meroni et al. (2022), we consider the anomalies of the along-wind ($\hat{r}$) and across-wind ($\hat{s}$) divergence components with respect to the background wind as a function of the $\hat{r}$ component of the SST gradient and the $\hat{s}$ component of the SST Laplacian for DMM and PA, respectively. This local geometrical transformation is actually useful since the wind response to PA might be offset from SST features due to advection as discussed in Lambaerts et al. (2013), Foussard et al. (2019), and Meroni et al. (2022). Indeed, the PA-mediated secondary circulation develops in response to the underlying SST structures on a length scale $L \sim Uh^2/K_T$, where U is the background wind speed, h is the MABL thickness, and K_T is the thermal eddy turbulent coefficient (see also Small et al. 2008). In the across background wind direction, U tends toward zero, reducing the length scale at which the response in wind develops and can be detected. It is worth noting that the use of the across-wind component of the

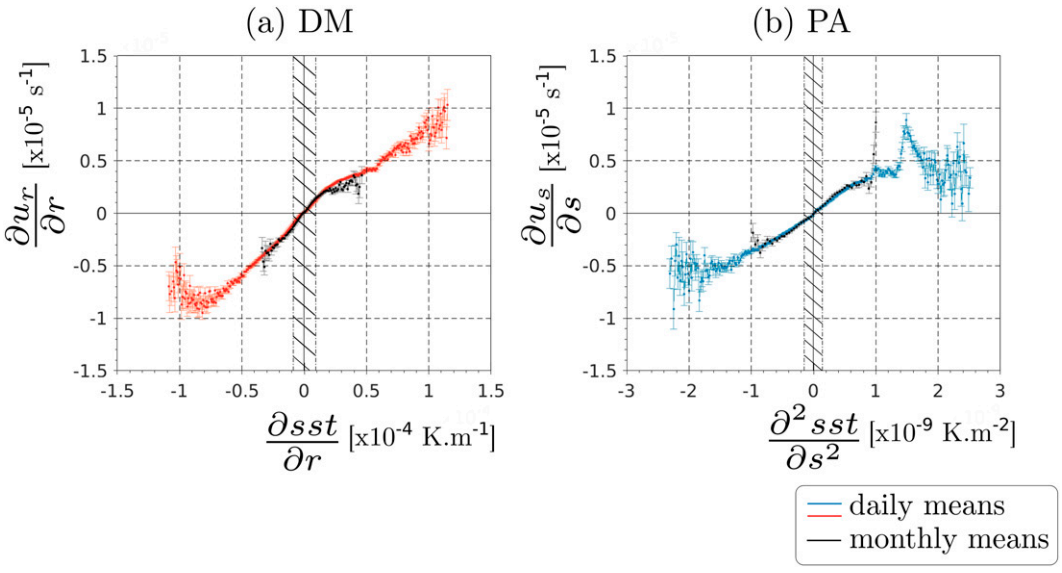

FIG. 2. Binned scatterplot of (a) the divergence of the wind anomaly in the along-wind direction as a function of the along-wind SST gradient and (b) the divergence of the wind anomaly in the across-wind direction as a function of the across-wind component of the SST Laplacian. Each dot and the corresponding error bar represent the mean and the standard error of the values in the corresponding bin. A total of 1000 bins of equal width have been used, from the minimum to the maximum value of the abscissa; only bins with more than 100 data points are shown. The red and blue colors ins (a) and (b) highlight the daily means; the black color in both panels is used for the monthly means. Red and blue shades are used throughout the manuscript to describe DMM and PA, respectively. The hatched area in both panels delimits the 90th centered percentiles of the SST derivatives.

second derivative of the SST reduces the effects of advection in the along-wind direction and the correlation with the corresponding wind divergence field amplifies. Thus, the PA-mediated response is more detectable [see Fig. 10 of Meroni et al. (2022) and the associated discussion for more details]. For clarity and consistency, we use the same frame of reference for DMM and define the relationship on to the $\hat{r}$ direction. Please note that the use of the classic metrics for DMM does not change the results.

Following Desbiolles et al. (2021), we compute the coupling coefficients between the relevant variables using bins with a fixed number of values: data are divided into percentile classes (5% of data in each class) of SST derivatives (the along-wind SST gradient for DMM and the across-wind SST Laplacian for PA), then the mean wind divergence is computed for each class and a linear regression is performed on the resulting 20 values. This method allows to compute the regression coefficient (hereafter called coupling coefficient, α_{DM} and α_{PA}), giving equal weight to the data while reducing the noise associated with the atmospheric variability.

Two main environmental conditions are considered in the following: the background wind speed, introduced above, and air–sea temperature difference. The latter is computed as $T_{air} - T_{oc}$, with T_{air} being the large-scale air temperature at 2 m above the surface and the large-scale T_{oc} the oceanic surface temperature, i.e., the low-pass filtered SST. As for the wind speed, the background air–sea temperature difference results from the same filtering process of the atmospheric and oceanic temperature fields (i.e., Lanczos filter, with a 2D half-power cutoff wavelength of 10°). The background air–sea temperature difference is considered as a good proxy of air-column stability (e.g., Kettle 2015). Indeed, since horizontal heterogeneity in the fields is removed at the small scales, the 1D conceptual model of the MABL can be considered: when the ocean is warmer than the overlaying atmosphere, the latter is heated by the ocean and the vertical transport is enhanced. Then, unstable (stable) conditions, corresponding to important negative (positive) values of $\Delta T = T_{air} - T_{oc}$, favor (inhibit) vertical transport through the atmosphere. The diagram $U - \Delta T$, commonly used to interpret air–sea interface conditions, is also used in this work.

3. Environmental control of thermal feedback

As noted in section 1, the relevant time scales over which DMM and PA mechanisms act are still being discussed in the recent literature. Here, the focus is on daily time scales and the statistics obtained with daily averaged fields are compared with those computed with the standard approach of using fields averaged on monthly (or longer) time scales (e.g., Chelton et al. 2001; O'Neill et al. 2005). In particular, Fig. 2a shows the binned scatterplot of the anomaly of the wind divergence in the along-wind direction, $\partial u_r/\partial r$, as a function of the along-wind component of the local SST gradient, $\partial sst/\partial r$. Figure 2b shows the corresponding figure for the PA mechanisms, with the wind divergence in the across-wind direction ($\partial u_s/\partial s$) as a function of the across large scale wind component of the SST Laplacian, $\partial^2 sst/\partial s^2$. Both panels are computed using data from the global ocean. Black and red dots show the mean of at least 100 observations of daily and

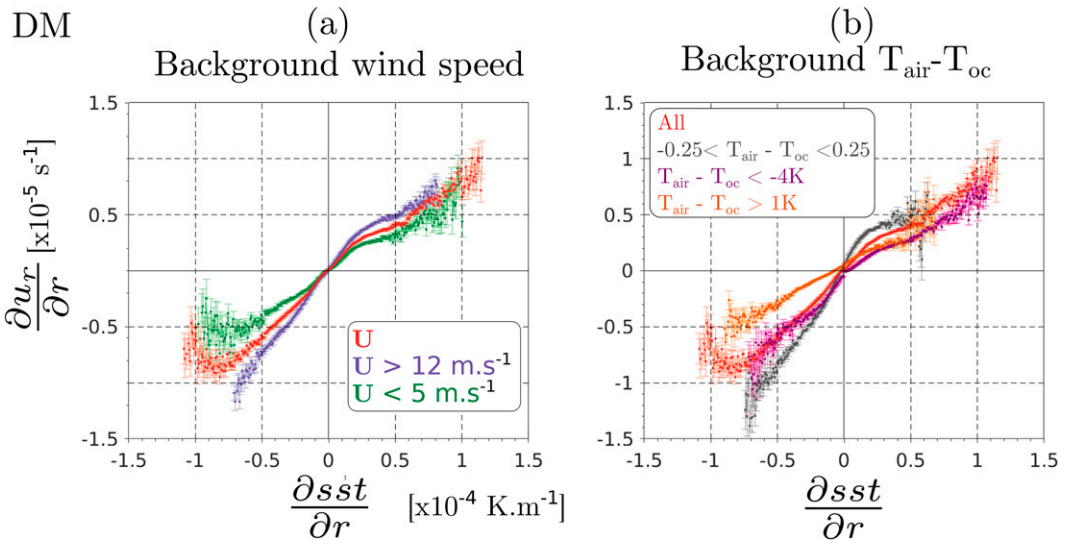

FIG. 3. As in Fig. 2a, with the discrimination of the data based on (a) background wind speed and (b) background air–sea temperature difference. In both panels, the red lines and points represent the binned distributions based on the full dataset and are strictly the same. In (a), the green and violet colors represent the data with the background wind speed lower than 5 m s^{-1} and greater than 12 m s^{-1}, respectively. In (b), the gray line shows data with a near-neutral stability, while the purple and orange colors are used for very unstable and very stable conditions, respectively, as indicated in the legend.

monthly means, respectively. Error bars represent the standard errors with respect to the corresponding means. Black hatched areas represent the interval in which 90% of the points of SST derivatives associated to DMM and PA are observed.

Figure 2 reveals that within the framework described in the previous section, the linear description of the DMM and PA relationships is a valid approximation for most of the points, both at daily and monthly time scales, consistent with previous literature (Chelton et al. 2001, 2004; O'Neill et al. 2005, 2012). However, over large forcing values, the linear relationship does not hold anymore for both mechanisms. In particular, for values of the along-wind component of SST gradient just outside of the bulk range (defined as the central 90% of the distribution and shown in the figure as the hatched region), both daily and monthly means depart from the linear behavior (see Fig. 2a). It is worth noting that the linear relationship remains valid for relatively large negative gradients, of the order of -0.5×10^{-4} K m^{-1}. This might be related to the fact that over the positive part of the plot, the wind divergence is produced by the reduction of the air column stability and the acceleration of the surface wind over warmer water. In the case of a well-mixed marine atmospheric boundary layer, an increase in instability and vertical mixing produces small effects on surface winds. On the contrary, an increase in stability, when the wind blows from warm to cold waters (negative ∂sst/∂r), has been shown to produce an internal boundary layer (Skyllingstad et al. 2007), which is a robust feature that breaks the link of the surface wind with the winds aloft. For the PA (Fig. 2b), the linear relationship looks more symmetrical between positive and negative values of the SST Laplacian. A detailed characterization of the nonlinearities goes beyond the scope of the present work and will be the object of future analyses.

Figure 3 shows the binned scatterplot for the DMM mechanism for different wind conditions (Fig. 3a) and air–sea temperature differences (Fig. 3b). The DMM coupling coefficient, given by the slope of the linear regression of the binned scatterplot, depends on both background wind speed conditions and air–sea temperature difference. More precisely, it is found that the coupling coefficient is larger at larger wind speeds, suggesting that the atmospheric response to the same downwind SST gradient is greater when the background wind is more intense (see, e.g., the comparison between red and blue lines showing the binned scatterplot for background wind greater than 12 m s^{-1} and less than 5 m s^{-1}, respectively, in Fig. 3a). This result could be related to the fact that the momentum mixing in the boundary layer is larger at larger winds, as the size of the turbulent eddies increases. When the discrimination is done based on the background air–sea temperature difference, the coupling coefficient associated with the DMM reaches the highest values for near-neutral conditions (gray line on Fig. 3b) and the lowest for very unstable (pink line) or stable large-scale conditions (orange line). This result is interpreted based on the fact that the turbulent mixing within the MABL is influenced by the air-column stability, resulting in excitation (inhibition) of large eddies in the presence of large-scale unstable (stable) conditions (Ma et al. 2015). When the large-scale conditions are near neutral stability, a local SST gradient will strongly impact the local vertical mixing, resulting in enhanced turbulence in the cold-to-warm transition or in the development of a stable internal boundary layer in the warm-to-cold transition (Kilpatrick et al. 2014). Conversely, in the presence of both

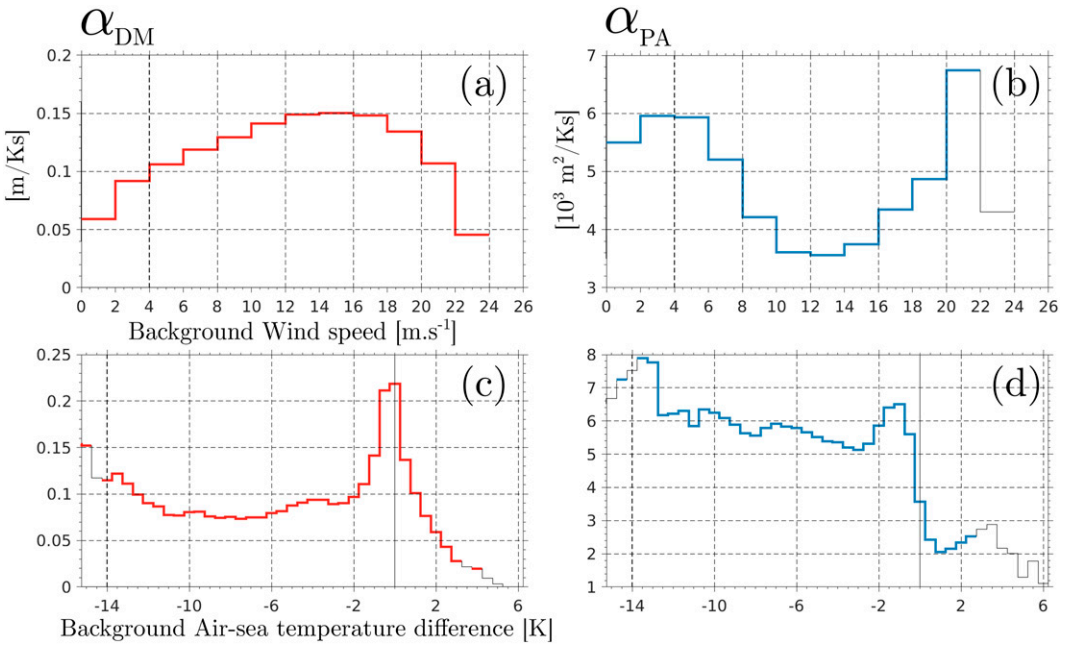

FIG. 4. Coupling coefficient (a),(b) α_{DM} (red lines) and (c),(d) α_{PA} (blue lines) as a function of (a),(c) background wind speed and (b),(d) background air–sea temperature difference. Solid colored lines indicate linear regression slopes that are statistically significant at the 95% confidence level.

strongly stable and strongly unstable large-scale conditions in the air column, the sensitivity of MABL mixing to local SST gradients is small. Another important feature revealed in Fig. 3b is the early drop of the linear dependence for stable conditions (orange line) compared to unstable conditions (purple line) for positive $\partial \mathrm{sst}/\partial r$. For very unstable conditions, defined here as $T_{air} - T_{oc} < -4$ K, the coupling between the wind above the MABL and the weakly sheared MABL winds is important and the entrainment of downward momentum flux is then enhanced over warmer SST. On the contrary, when the air column is very stable ($T_{air} - T_{oc} > +1$ K), the thermal feedback disappears since there is no entrainment at the top of the MABL: with a very sheared MABL upper-level winds are essentially decoupled from the boundary layer dynamics.

Figure 3 can be extended by computing the coupling coefficient to highlight the dependence on the relevant environmental conditions. Figure 4 displays α_{DM} (Figs. 4a,b, red lines) and α_{PA} (Figs. 4c,d, blue lines) as a function of the background wind speed (Figs. 4a,c) and background air–sea temperature difference (Figs. 4b,d), using bins of 2 m s^{-1} and 0.5 K, respectively. Starting from the DMM mechanism, the behavior observed in Fig. 3 is found to smoothly apply both as a function of the background wind and as a function of the background air–sea temperature difference. For most values of background wind speed, in fact, the DMM coupling coefficient increases with wind, and a relatively sharp drop is found for very high wind speed. We suggest that the behavior at low and moderate winds might arise from the MABL turbulent mixing increase with wind speed and then, for large enough winds, the drop in the advective time scale, L/U with L being the length scale of the SST variation, becomes dominant. In those latter conditions, the time interval in which the air parcel is in contact with the SST forcing structure decreases with increasing U, possibly resulting in a drop of the regression coefficient. Further analysis will be necessary in subsequent works in order to verify the given interpretation. In terms of the dependence on the atmospheric stability, the DMM coupling coefficient is found to peak in near-neutral conditions, confirming that the strongest atmospheric response is found when the crossing of an SST front happens near neutrally stable conditions (Figs. 4a,b).

The PA coupling coefficient, shown in Fig. 4d, admits two significantly different behaviors over negative and positive air–sea temperature differences. The variability in both regimes, i.e., unstable and stable, respectively, is very low. The low values of α_{PA} for stable conditions are interpreted as due to the weaker reactivity of a stable atmosphere, where temperature anomalies do not rapidly diffuse in the lower troposphere. On the contrary, when the air column is unstable, surface temperature anomalies can quickly affect the MABL density and thus modify the pressure field, resulting in a stronger PA-mediated coupling. In terms of the dependence of α_{PA} on U (Fig. 4c), two peaks are well marked at low background winds (between 2 and 6 m s^{-1}) and strong background winds (faster than 18 m s^{-1}). This will be discussed below. Note that few observations are made with background winds stronger than 22 m s^{-1} since U is the daily mean large-scale wind (which is the reason why the coupling coefficient is not statistically significant in the last U bin of this panel).

These diagnostics can be generalized by simultaneously taking into account the large-scale surface wind speed and the stability of the air column. This is shown in Fig. 5, which

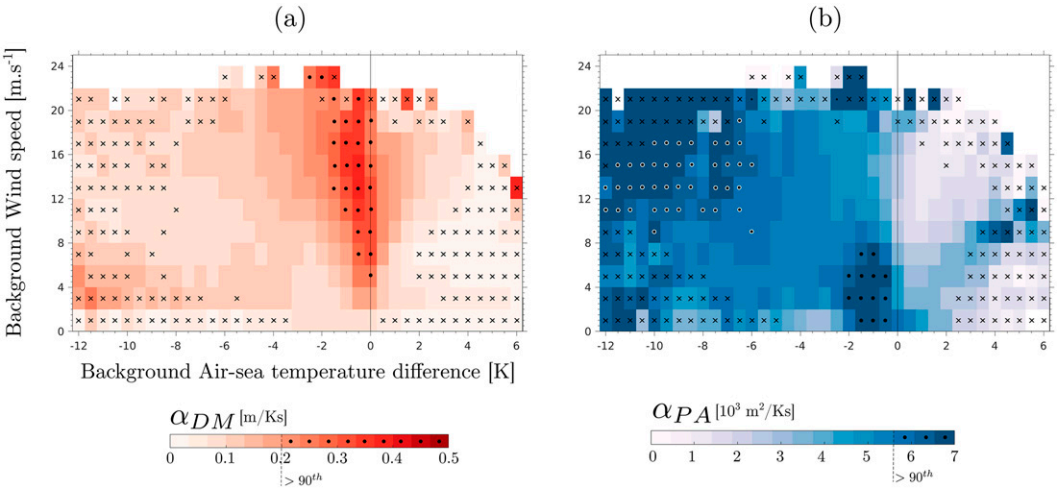

FIG. 5. Coupling coefficient (a) α_{DM} and (b) α_{PA} in a 2D frame: the x and y axes represent the background air–sea temperature difference and the background wind speed, respectively. The cross symbol indicates that the null hypothesis of regression coefficient equal to zero cannot be rejected at the 95% confidence level. Dot symbols highlight the 10% highest percentiles of each coupling coefficient (used to define the favorable environmental conditions; see text for details). In (b), black dots with white contours represent conditions in which THF-driven PA mechanism occurs (see section 4 and Fig. 7).

represents the coupling coefficients α_{DM} (Fig. 5a) and α_{PA} (Fig. 5b) as a function of the large-scale air–sea temperature difference (x axis) and the background wind speed (y axis). The cross symbols indicate a nonsignificant linear regression at 95% confidence level and the dots highlight the 10% highest coupling coefficients. The higher the coupling coefficient, the more the process is able to constrain the atmospheric dynamics (either in terms of the along-wind component of the divergence, or the across-wind counterpart). The DMM is most efficient, for a given SST gradient, for moderate-to-high wind regimes in a near-neutral atmospheric column. Indeed, the 10% highest values of α_{DM} are found for background air–sea temperature difference between -1 and 0.5 K and large-scale wind speed from 4 up to 20 m s^{-1} (Fig. 5a). This result has been already commented above and confirms the sensitivity of DMM to one parameter only highlighted in Fig. 5.

On top of the already-described dependence of α_{PA} on air–sea thermal disequilibrium, Fig. 5b highlights that the environmental conditions that promote the efficiency of PA mechanism in shaping the atmospheric divergence/convergence cells across SST structures involve two separate regimes: 1) a low-wind regime in slightly unstable to near-neutral conditions and 2) a high-wind regime with very unstable air columns. To interpret those results, we introduce the PA mechanism characteristics time scale, typically considered as the diffusive time scale h^2/K_T, where h is the boundary layer thickness and K_T is the temperature eddy diffusion coefficient (Small et al. 2008). Considering that K_T depends on stability and it has larger values for unstable air columns (ECMWF 2016), it is clear that for unstable atmospheric profiles (negative values of $T_{air} - T_{oc}$) the shorter time scale for pressure to adjust to local SST allows for a greater coupling coefficient. The interpretation is further supported by the fact that in stable conditions the largest values of α_{PA} are obtained for very weak winds, when the air resides for long times over the same surface thermal structures and it thus has time to adjust to local SST, even if K_T is small. The same reasoning holds also for slightly unstable conditions, and it results in very large coupling coefficients for small negative air–sea temperature differences. In those cases, the ratio between the advective time scale L/U and the PA characteristic time scale h^2/K_T—resulting in an adimensional number $(K_T L)/(h^2 U)$—is large, driven by the small U in the denominator. In a low-wind regime in slightly unstable to near-neutral conditions the air pressure is able to adjust to the local minima (maxima) of SST and develop the secondary circulation with the creation of local diverging (converging) cells, as discussed by Lambaerts et al. (2013) and Foussard et al. (2019). We hypothesize that the smaller values found for low winds in more unstable conditions are related to the thicker boundary layer (large h), which is typically associated with warm SST (Businger and Shaw 1984; Wai and Stage 1989), that increases the diffusion time scale. This hypothesis implies that at large air–sea thermal disequilibrium the increase in h^2 dominates over the increase of K_T with instability in determining the overall change of the diffusive time scale. This framework, however, cannot explain the existence of the separate regime with large values of α_{PA}, clearly evident in Fig. 5b, characterized by strong background winds and very unstable air columns. We justify the presence of this second regime considering that the temperature anomaly developing at a given height in the boundary layer (and thus the corresponding pressure anomaly) depends on the vertical turbulent transport of heat previously considered and also on the bottom boundary condition, i.e., the air–sea heat flux. In other words, a large pressure anomaly can be obtained either because diffusion acts for a long enough time to homogenize the boundary layer and/or

because it acts for a shorter time but on large vertical temperature gradients, the latter situation being maintained by strong bottom fluxes. Indeed, the second regime with an efficient PA mechanism in response to SST patterns appears at very large air–sea sensible heat exchanges, expressed in the bulk formula as the product of wind speed by the thermal disequilibrium between water and air (Fairall et al. 2003). This interpretation indicates that the efficiency of the PA mechanism in developing secondary circulations in response to SST structures should be expressed in term of the arising baroclinic pressure anomaly [in line with what has been done in Schneider and Qiu (2015)], and not only of the advection and diffusion time scales. In summary, for the same SST structure, different pressure anomalies arise depending on MABL height, air column stability, wind speed, and surface heat fluxes, which are interlinked in nontrivial ways. The full exploration of those drivers goes beyond the scope of this paper.

4. Frequency and location of environmental-favored DMM and PA conditions and rainfall response

The coupling coefficients computed as a function of large-scale air–sea temperature difference and background wind speed are used to define favorable environmental conditions for DMM and PA mechanisms. More precisely, when a coupling coefficient is equal to or greater than the 90% percentile of its distribution, marked as a dot in Fig. 5, a favorable environmental condition is identified. Those conditions thus correspond to the range of covariability of large-scale air–sea temperature difference and background wind for which each process potentially exert the strongest influence on wind divergence structures in the MABL (either in the along- or across-wind direction, according to the mechanism considered).

By counting the number of points satisfying both the large-scale air–sea temperature difference and background wind speed, using the 5-yr daily averaged maps considered and by normalizing it by the number of total days in the same period, one obtains a map of frequency of occurrence of environmental conditions that favor DMM and PA the most. Figure 6 shows such maps for DMM (Fig. 6a, red shading) and PA (Fig. 6b, blue shading). On the top of the colored shading, isolines of occurrences of significant SST structures [along-wind component of the local SST gradient and across-wind component of the SST Laplacian for DMM (Fig. 6a) and PA (Fig. 6b), respectively] are drawn. More precisely, isolines show the frequency of occurrence of local SST structure in the upper quartile of the global distribution. Patterns of occurrence of favorable conditions for DMM are present mostly from mid- to high latitudes. This is not surprising since the DMM depends upon the background wind speed, which is stronger at higher latitudes (note the high occurrence of DMM-favoring conditions over the Southern Ocean which admits large SST gradients). High coupling coefficients for DMM are also found for near-neutral air columns concomitant with wind speed from 6 to 20 m s^{-1}. As a consequence, DMM-mediated responses are very frequent in the upwelling systems, as highlighted in Fig. 6a. This is true for the four major EBUSs, the Somalian coast, and the eastern Australian one. The eastern Pacific cold tongue emerges to

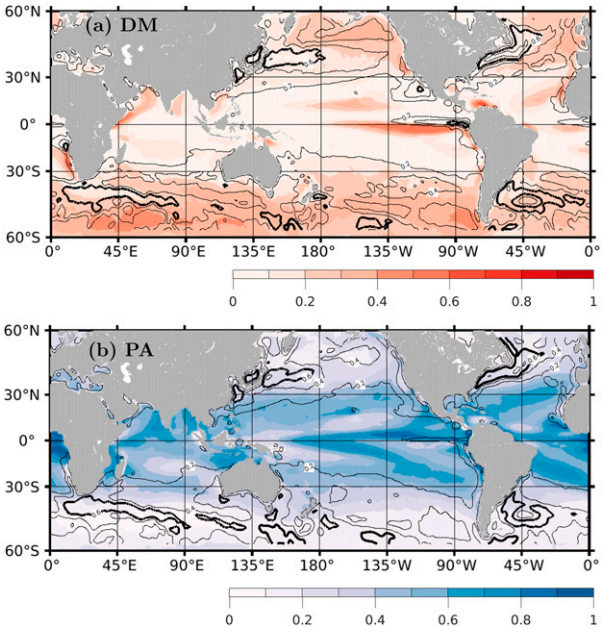

FIG. 6. Frequency of occurrence of favorable environmental conditions for (a) DMM and (b) PA (colors). Contours show the frequency of occurrence of (a) $|\partial \mathrm{sst}/\partial r|$ and (b) $|\partial^2 \mathrm{sst}/\partial s^2|$ in the upper quartile of $|\partial \mathrm{sst}/\partial r|$ and $|\partial^2 \mathrm{sst}/\partial s^2|$ for DMM and PA, respectively. Please note that the contour lines have been filtered for the clarity of the figure. The contour interval is 0.2 from 0.2 to 0.8. The isoline corresponding to the 0.6 frequency is highlighted with a bold line.

frequently favor the DMM-mediated response. In particular, in this region, even if the wind is steadily weak (trade wind regime), the relative cool temperature of the sea reduces the air–sea temperature difference and, with these near-neutral conditions, the atmosphere becomes very sensitive to SST gradients [which can be very strong if tropical instability waves are present, as shown in Chelton et al. (2001)]. The relationship between α_{DM} and background wind speed is pretty clear and naturally highlights the predominance of DMM at high latitudes.

The PA-mediated response is favored over two distinctive regimes (see Fig. 5). The relative occurrence of favorable conditions for PA mechanism depicted in Fig. 6b is dominated by the marginally unstable/low wind regime and, therefore, its pattern highlights the low-latitude band between +30° and −30°, characterized by trade winds and warm waters. However, those regions do not frequently exhibit significant thermal heterogeneity.

The second atmospheric condition which favors the PA-mediated response, associated with strong winds (>12 m s^{-1}) and important negative air–sea temperature differences (cold air over warm water, i.e., highly unstable air masses), is highlighted by white circles in Fig. 5 and corresponds to intense air–sea THFs. In Fig. 7 the frequency of occurrence of those conditions is shown together with the frequency of having large across-wind SST Laplacians. As in these environmental conditions (i.e., large negative background air–sea temperature difference and intense background winds), the air–sea THFs are particularly strong; they are named THF-

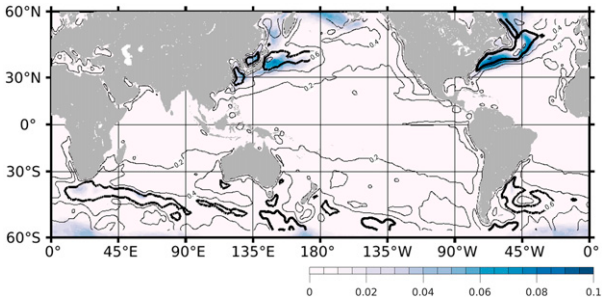

FIG. 7. Frequency of occurrence of favorable environmental conditions for THF-driven PA mechanism (colors). Contours (same as Fig. 6b) show the frequency of occurrence of values of $|\partial^2 \mathrm{sst}/\partial s^2|$ in the upper quartile of its distribution. Please note that the contour lines have been filtered for the clarity of the figure. The contour interval is 0.2 from 0.2 to 0.8. The isoline corresponding to the 0.6 frequency is highlighted with a bold line.

driven PA conditions. It appears that the THF-driven PA conditions only happen over WBCs and their extensions, especially when cold dry air masses arriving from the continent blow over the warm currents, inducing very large heat fluxes from the ocean into the atmosphere. Indeed, these conditions are observed during boreal and austral winters in the Northern and Southern Hemispheres, respectively (see Fig. S3 of the supplemental material). The THF-driven PA conditions during the winter season are naturally less frequent than the other PA-mediated favorable conditions (see Figs. 6b and 7) since both the corresponding large negative background air–sea temperature difference and intense background winds are in the tails of their respective distribution (not shown). It is worth noting here that over WBCs, both environmental-favorable PA-mediated regimes are present with a frequency of the same order of magnitude (~10%, see Figs. 6b and 7). To the best of our knowledge, this is an aspect that has been overlooked in the literature, as the PA-driven atmospheric response has previously been shown to act over WBCs only over long time scales (Minobe et al. 2008).

So far, the PA- and DMM-mediated responses have been isolated and the corresponding favoring conditions have been defined when the concomitant background wind speed and air–sea temperature difference conditions promote the wind response (top 10% of the coupling coefficient values). The statistical local low-cloud cover and rainfall responses during those conditions are now analyzed and categorized according to the sign of the respective SST derivative ($\partial \mathrm{SST}/\partial r$ and $\partial^2 \mathrm{SST}/\partial s^2$ for DMM and PA, respectively). Indeed, as noticed above, following the DMM mechanism, a positive (negative) along-wind SST gradient favors the development of a surface diverging (converging) cell in the MABL. For the PA mechanism, instead, a local maximum (minimum) of SST, induced by a negative (positive) SST Laplacian, produces a surface converging (diverging) cell in the MABL. The presence of a converging cell can generate upward motion and, thus, enhance cloud formation and rainfall. Desbiolles et al. (2021) have shown that over the Mediterranean Sea there is a statistical response in agreement with this picture, proving that the

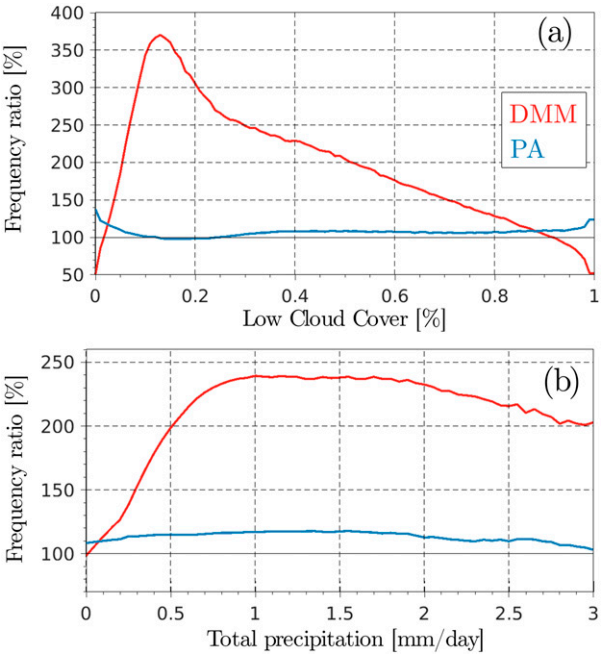

FIG. 8. Ratio of daily (a) low-cloud cover and (b) precipitation pdfs over convergence- and divergence-inducing SST structures for DMM (red) and PA (blue) mechanisms. It has been computed as the ratio between the pdf of low-cloud cover and rainfall conditioned to the uppermost and to the lowermost quartiles of $\partial \mathrm{SST}/\partial r$ and $\partial^2 \mathrm{SST}/\partial s^2$ for the environmentally favored DMM and PA conditions, respectively.

presence of mesoscale SST structures can affect low-level cloud cover and rainfall over daily time scales. Here we extend the analysis shown in Desbiolles et al. (2021) to the global ocean, considering both DMM and PA mechanisms.

The pdf (probability density function) of daily low-cloud cover and rainfall are computed (see Fig. S4). By conditioning the pdf to some values of the relevant SST forcing fields, one can infer the relevance of the mechanism considered in affecting cloud cover and precipitation in a statistical sense. In particular, the ratio between such conditioned pdfs is used as an indicator of whether the presence of mesoscale SST structures affects the above atmospheric dynamics.

Figure 8 shows the ratio of the pdfs of low-cloud cover and precipitation conditioned to the uppermost and the lowermost quartiles of $\partial \mathrm{SST}/\partial r$ and $\partial^2 \mathrm{SST}/\partial s^2$ for the DMM (red) and PA (blue), respectively. A ratio equal to 1 (100%) indicates that the chances of having a given amount of precipitation over convergence- and divergence-inducing SST structures are identical. The figure shows an enhancement of frequency of cloud cover and precipitation over convergence-inducing SST structures for DMM: the chances of having rainfall larger than 0.5 mm day^{-1} are more than doubled in response to the mesoscale SST forcing. For PA, the enhancement of frequency of precipitation varies from 10% to 20%. This relatively small signal might be due to the fact that advection can displace the precipitation from the convection-inducing SST structure, as described in Foussard et al. (2019).

5. Concluding remarks

In this study, ERA5 data have been used to investigate the environmental conditions that favor thermal feedback mechanisms in forcing diverging/converging cells in the MABL at daily time scales. The analysis throughout the paper is based on a classical approach of a linear regression between wind divergence and SST structures (along-wind gradients and across-wind Laplacian components for DMM and PA, respectively). Even if that initial hypothesis is discussed in the paper and the present analysis and interpretation consider other aspects (see below and section 3), it is worth to recall here that the existence of a significant linear correlation represents an initial insight on the thermal feedback processes at play and further analysis might improve the identification of the relevant processes at play. As already initiated by other authors (e.g., Lambaerts et al. 2013; Foussard et al. 2019), our approach examines the dependencies of the linear regression on large-scale atmospheric conditions over the global ocean. Therefore, the results might give useful guidance on the interpretation of the effects of thermal feedback on MABL dynamics. Specifically, it is found that both mechanisms (DMM and PA) act over a wide range of background wind speed and atmospheric stability conditions. The variability of these two variables has been predefined here as the main control of the thermal feedback processes since they control the air–sea turbulent fluxes of heat, water vapor, and momentum, as previously highlighted by Smith (1988). Indeed, the large organized eddies in the MABL, linked to the turbulence state, are affected by the background wind speed and by the large-scale air–sea temperature difference, used as a proxy of air-column stability.

Using classical computations linking the monthly-averaged wind speed and SST perturbations to highlight DMM, it is found that ERA5 coupling coefficients are comparable to those found in the literature using satellite data over specific areas such as WBC systems (O'Neill et al. 2010; Desbiolles et al. 2018). Moreover, in this study, the binned scatterplots between metrics highlighting the action of DMM and PA mechanisms show a linear behavior for most of the observations of SST gradient or SST Laplacian (see Fig. 2). Linear regression based on daily mean fields, i.e., daily coupling coefficients, and on monthly means are almost identical (see Fig. 2). The advantage of using daily data is that the range of variables explored is wider both in terms of forcing and in terms of response fields. The arguments mentioned above suggest that, despite that the daily atmospheric fields are noisier than their long-term averaged counterparts, the air–sea coupling happens on short time scales, as suggested by recent studies using large-eddy simulations (LES) (e.g., Wenegrat and Arthur 2018; Sullivan et al. 2021). Over extreme SST forcings, however, the linear dependence of the diverging/converging cells of the low-level atmosphere does not hold anymore. In the case of DMM, this is especially true for winds blowing from cold to warm SST (positive downwind SST gradient) for which an abrupt disruption of the linear dependence is seen over moderately large values. Future efforts should be devoted to a full characterization of these nonlinearities.

However, for the majority of the observations it is found that the linear approximation is valid (see Fig. 2) and the coupling coefficient depends upon environmental conditions. More precisely, the DMM is favored for low air–sea temperature differences (near-neutral stability) and a background wind speed varying from 6 to 20 m s^{-1}. Most of the environmentally favored DMM conditions are located from mid- to high latitudes and with an important occurrence in the EBUSs, where the air column is often in near-neutral or marginally stable conditions. The PA-mediated response is overall more important in unstable air columns, and in particular it is more efficient in two distinct regimes: 1) high background wind speed and very unstable air columns and 2) low wind speed and slightly unstable air columns. The first regime can be interpreted considering the large heat fluxes that ensue at the air–sea interface, and the second one by the fact that the air parcel spends a long time over the SST forcing structures: in both cases a large baroclinic pressure anomaly can develop and drive a secondary circulation across the thermal front.

The simultaneous occurrence of high background wind speed and unstable conditions is observed over WBCs (especially during cold-air outbreaks) and in the Southern Ocean. This result suggests that not only is PA important over annual time scale in these areas (e.g., Minobe et al. 2008) but potentially exerts an important influence at daily time scales also. The highly dynamical nature of those regions demands for a careful quantification of the specific role of PA in shaping divergence/convergence cells. The other environmental favorable conditions for PA mechanism are located in the tropical band between +30° and −30° latitude, which is usually characterized by marginally unstable air column with relatively weak trade winds (see Fig. 6b).

By analyzing the response in terms of rainfall probability to the uppermost and lowermost SST forcing, a clear signal emerge. In particular, the convergence-favoring mesoscale SST structures correspond to a doubling of the probability of producing strong rainfall (>0.5 mm day^{-1}) with respect to the probability associated to divergence-favoring SST structures for the DMM mechanism. The enhancement of cloud cover and of precipitation over SST structures through the PA mechanism is much smaller, possibly due to the displacement of the response due to advection.

The results presented here are limited to relatively large structures, due to the resolution of the data. Extension of the work to smaller scales, through the direct use of high resolution SST and wind observational products will shed light onto the air–sea coupling at finer scales, of paramount importance for the development of sub grid parameterizations.

Acknowledgments. We thank two anonymous reviewers for their valuable contributions that allowed us to improve the manuscript substantially. The authors acknowledge support from the project JPI Climate Oceans EUREC4A-OA, Progetto Dipartimenti di Eccellenza, funded by MIUR 2018-2022. FD has been supported by Piano Operativo Nazionale "Ricerca e Innovazione," Italian Ministry of University and Research, RTDAPON-150, with collaboration between Milano-Bicocca and CIMA Research Foundation. ANM is supported by the

European Space Agency (ESA) as part of the GLAUCO Climate Change Initiative (CCI) fellowship (ESA ESRIN/Contract 4000133281/20/I/NB). LR is supported by Institute de Recherche et de Developpement (IRD).

Data availability statement. ERA5 data used in this study have been freely downloaded from the Copernicus server (https://cds.climate.copernicus.eu/cdsapp#!/dataset/reanalysis-era5-single-levels?tab=overview). CDO tools have been used to calculate the daily means from the available hourly outputs. Postprocessing analyses have been performed with MATLAB. All the MATLAB codes are available on the GitHub server: https://github.com/FabienDesbiolles/J.Clim.2022.git.

APPENDIX

Local Cartesian Frame of Reference and Associated Definitions

The components of the background horizontal wind at 10 m are used to introduce a frame of reference that simplifies the detection of the DMM- and PA-mediated atmospheric response (Meroni et al. 2022). We define a local Cartesian frame of reference $\{\hat{r}, \hat{s}\}$ based on this large-scale wind vector $\mathbf{U} = (U, V)$, with $\hat{r}$ being the along-wind unit vector and $\hat{s}$ the across-wind unit vector (positive at 90° counterclockwise with respect to $\hat{r}$).

Formally, in the standard local Cartesian frame of reference, the local wind $\mathbf{u} = (u, v)$ is the sum of the large-scale wind (U, V) and an anomaly (u', v'), so that

$$u = U + u'; \quad v = V + v'. \tag{A1}$$

In the new frame of reference, the wind field is

$$\dot{r} = u\cos\phi + v\sin\phi; \quad \dot{s} = -u\sin\phi + v\cos\phi, \tag{A2}$$

with $\cos\phi = U/\sqrt{U^2 + V^2}$ and $\sin\phi = V/\sqrt{U^2 + V^2}$ and, by definition, it can be decomposed as

$$\dot{r} = \sqrt{U^2 + V^2} + u_r; \quad \dot{s} = u_s. \tag{A3}$$

By projecting the gradient $\nabla\psi$ of a given scalar quantity ψ, onto the new directions $\{\hat{r}, \hat{s}\}$, the derivatives with respect to r and s are

$$\frac{\partial\psi}{\partial r} = \hat{\mathbf{r}}\cdot\nabla\psi; \quad \frac{\partial\psi}{\partial s} = \hat{\mathbf{s}}\cdot\nabla\psi. \tag{A4}$$

In particular, using $\{\varphi, \theta\}$ to denote longitude and latitude, the local rotation with respect to the large-scale wind gives

$$\frac{\partial\psi}{\partial r} = \frac{\cos\phi}{R\cos\theta}\frac{\partial\psi}{\partial\varphi} + \frac{\sin\phi}{R}\frac{\partial\psi}{\partial\theta}; \tag{A5}$$

$$\frac{\partial\psi}{\partial s} = \frac{-\sin\phi}{R\cos\theta}\frac{\partial\psi}{\partial\varphi} + \frac{\cos\phi}{R}\frac{\partial\psi}{\partial\theta}. \tag{A6}$$

With these, the SST forcing fields for DMM and PA are, respectively, the along-wind SST gradient

$$\frac{\partial\mathrm{sst}}{\partial r} = \frac{\cos\phi}{R\cos\theta}\frac{\partial\mathrm{sst}}{\partial\varphi} + \frac{\sin\phi}{R}\frac{\partial\mathrm{sst}}{\partial\theta} \tag{A7}$$

and the across-wind SST Laplacian

$$\frac{\partial^2\mathrm{sst}}{\partial s^2} = \frac{\sin^2\phi}{R^2\cos^2\theta}\frac{\partial^2\mathrm{sst}}{\partial\varphi^2} - 2\frac{\sin\phi\cos\phi}{R^2\cos\theta}\frac{\partial^2\mathrm{sst}}{\partial\varphi\partial\theta} - \frac{\sin\phi\cos\phi}{R^2}\frac{\sin\theta}{\cos^2\theta}\frac{\partial\mathrm{sst}}{\partial\varphi} + \frac{\cos^2\phi}{R^2}\frac{\partial^2\mathrm{sst}}{\partial\theta^2}. \tag{A8}$$

The response fields for DMM and PA are, instead, the along-wind derivative of the along-wind wind anomaly

$$\frac{\partial u_r}{\partial r} = \frac{\cos\phi}{R\cos\theta}\frac{\partial u_r}{\partial\varphi} + \frac{\sin\phi}{R}\frac{\partial u_r}{\partial\theta} \tag{A9}$$

and the across-wind derivative of the across-wind wind anomaly

$$\frac{\partial u_s}{\partial s} = \frac{-\sin\phi}{R\cos\theta}\frac{\partial u_s}{\partial\varphi} + \frac{\cos\phi}{R}\frac{\partial u_s}{\partial\theta}. \tag{A10}$$

REFERENCES

Bishop, S. P., R. J. Small, and F. O. Bryan, 2020: The global sink of available potential energy by mesoscale air-sea interaction. *J. Adv. Model. Earth Syst.*, **12**, e2020MS002118, https://doi.org/10.1029/2020MS002118.

Businger, J. A., and W. J. Shaw, 1984: The response of the marine boundary layer to mesoscale variations in sea-surface temperature. *Dyn. Atmos. Oceans*, **8**, 267–281, https://doi.org/10.1016/0377-0265(84)90012-5.

Buzzi, A., E. Di Muzio, and P. Malguzzi, 2020: Barrier winds in the Italian region and effects of moist processes. *Bull. Atmos. Sci. Technol.*, **1**, 59–90, https://doi.org/10.1007/s42865-020-00005-6.

Chelton, D. B., and S.-P. Xie, 2010: Coupled ocean-atmosphere interaction at oceanic mesoscales. *Oceanography*, **23**, 52–69, https://doi.org/10.5670/oceanog.2010.05.

——, and Coauthors, 2001: Observations of coupling between surface wind stress and sea surface temperature in the eastern tropical Pacific. *J. Climate*, **14**, 1479–1498, https://doi.org/10.1175/1520-0442(2001)014<1479:OOCBSW>2.0.CO;2.

——, M. G. Schlax, M. H. Freilich, and R. F. Milliff, 2004: Satellite measurements reveal persistent small-scale features in ocean winds. *Science*, **303**, 978–983, https://doi.org/10.1126/science.1091901.

——, ——, and R. M. Samelson, 2007: Summertime coupling between sea surface temperature and wind stress in the California Current System. *J. Phys. Oceanogr.*, **37**, 495–517, https://doi.org/10.1175/JPO3025.1.

Desbiolles, F., B. Blanke, A. Bentamy, and N. Grima, 2014: Origin of fine-scale wind stress curl structures in the Benguela and Canary upwelling systems. *J. Geophys. Res. Oceans*, **119**, 7931–7948, https://doi.org/10.1002/2014JC010015.

——, R. Blamey, S. Illig, R. James, R. Barimalala, L. Renault, and C. Reason, 2018: Upscaling impact of wind/sea surface temperature mesoscale interactions on southern Africa austral summer climate. *Int. J. Climatol.*, **38**, 4651–4660, https://doi.org/10.1002/joc.5726.

——, M. Alberti, M. E. Hamouda, A. N. Meroni, and C. Pasquero, 2021: Links between sea surface temperature structures, clouds and rainfall: Study case of the Mediterranean Sea. *Geophys. Res. Lett.*, **48**, e2020GL091839, https://doi.org/10.1029/2020GL091839.

Drobinski, P., S. Bastin, T. Arsouze, K. Beranger, E. Flaounas, and M. Stefanon, 2018: North-western Mediterranean sea-breeze circulation in a regional climate system model. *Climate Dyn.*, **51**, 1077–1093, https://doi.org/10.1007/s00382-017-3595-z.

ECMWF, 2016: IFS documentation part IV: Physical processes. ECMWF IFS Doc. Cy41r2, 213 pp., https://www.ecmwf.int/sites/default/files/elibrary/2016/16648-part-iv-physical-processes.pdf.

Fairall, C. W., E. F. Bradley, J. E. Hare, A. A. Grachev, and J. B. Edson, 2003: Bulk parameterization of air–sea fluxes: Updates and verification for the COARE algorithm. *J. Climate*, **16**, 571–591, https://doi.org/10.1175/1520-0442(2003)016<0571:BPOASF>2.0.CO;2.

Foussard, A., G. Lapeyre, and R. Plougonven, 2019: Response of surface wind divergence to mesoscale SST anomalies under different wind conditions. *J. Atmos. Sci.*, **76**, 2065–2082, https://doi.org/10.1175/JAS-D-18-0204.1.

Frenger, I., N. Gruber, R. Knutti, and M. Münnich, 2013: Imprint of Southern Ocean eddies on winds, clouds and rainfall. *Nat. Geosci.*, **6**, 608–612, https://doi.org/10.1038/ngeo1863.

Gentemann, C. L., and Coauthors, 2020: FluxSat: Measuring the ocean–atmosphere turbulent exchange of heat and moisture from space. *Remote Sens.*, **12**, 1796, https://doi.org/10.3390/rs12111796.

Hayes, S. P., M. J. McPhaden, and J. M. Wallace, 1989: The influence of sea-surface temperature on surface wind in the eastern equatorial Pacific: Weekly to monthly variability. *J. Climate*, **2**, 1500–1506, https://doi.org/10.1175/1520-0442(1989)002<1500:TIOSST>2.0.CO;2.

Hersbach, H., and Coauthors, 2020: The ERA5 global reanalysis. *Quart. J. Roy. Meteor. Soc.*, **146**, 1999–2049, https://doi.org/10.1002/qj.3803.

Kettle, A. J., 2015: A diagram of wind speed versus air-sea temperature difference to understand the marine atmospheric boundary layer. *Energy Procedia*, **76**, 138–147, https://doi.org/10.1016/j.egypro.2015.07.879.

Kilpatrick, T., N. Schneider, and B. Qiu, 2014: Boundary layer convergence induced by strong winds across a midlatitude SST front. *J. Climate*, **27**, 1698–1718, https://doi.org/10.1175/JCLI-D-13-00101.1.

Lambaerts, J., G. Lapeyre, R. Plougonven, and P. Klein, 2013: Atmospheric response to sea surface temperature mesoscale structures. *J. Geophys. Res. Atmos.*, **118**, 9611–9621, https://doi.org/10.1002/jgrd.50769.

Li, Y., and R. E. Carbone, 2012: Excitation of rainfall over the tropical western Pacific. *J. Atmos. Sci.*, **69**, 2983–2994, https://doi.org/10.1175/JAS-D-11-0245.1.

Lindzen, R. S., and S. Nigam, 1987: On the role of sea surface temperature gradients in forcing low-level winds and convergence in the tropics. *J. Atmos. Sci.*, **44**, 2418–2436, https://doi.org/10.1175/1520-0469(1987)044<2418:OTROSS>2.0.CO;2.

Ma, J., H. Xu, C. Dong, P. Lin, and Y. Liu, 2015: Atmospheric responses to oceanic eddies in the Kuroshio extension region. *J. Geophys. Res. Atmos.*, **120**, 6313–6330, https://doi.org/10.1002/2014JD022930.

Meroni, A. N., A. Parodi, and C. Pasquero, 2018: Role of SST patterns on surface wind modulation of a heavy midlatitude precipitation event. *J. Geophys. Res. Atmos.*, **123**, 9081–9096, https://doi.org/10.1029/2018JD028276.

——, M. Giurato, F. Ragone, and C. Pasquero, 2020: Observational evidence of the preferential occurrence of wind convergence over sea surface temperature fronts in the Mediterranean. *Quart. J. Roy. Meteor. Soc.*, **146**, 1443–1458, https://doi.org/10.1002/qj.3745.

——, F. Desbiolles, and C. Pasquero, 2022: Introducing a new metrics for the atmospheric pressure adjustment to thermal structures at the ocean surface. *J. Geophys. Res. Atmos.*, **127**, e2021JD035968, https://doi.org/10.1029/2021JD035968.

Minobe, S., A. Kuwano-Yoshida, N. Komori, S.-P. Xie, and R. J. Small, 2008: Influence of the Gulf Stream on the troposphere. *Nature*, **452**, 206–209, https://doi.org/10.1038/nature06690.

O'Neill, L. W., D. B. Chelton, and S. K. Esbensen, 2003: Observations of SST-induced perturbations of the wind stress field over the Southern Ocean on seasonal timescales. *J. Climate*, **16**, 2340–2354, https://doi.org/10.1175/2780.1.

——, ——, ——, and F. J. Wentz, 2005: High-resolution satellite measurements of the atmospheric boundary layer response to SST variations along the Agulhas return current. *J. Climate*, **18**, 2706–2723, https://doi.org/10.1175/JCLI3415.1.

——, ——, and ——, 2010: The effects of SST-induced surface wind speed and direction gradients on midlatitude surface vorticity and divergence. *J. Climate*, **23**, 255–281, https://doi.org/10.1175/2009JCLI2613.1.

——, ——, and ——, 2012: Covariability of surface wind and stress responses to sea surface temperature fronts. *J. Climate*, **25**, 5916–5942, https://doi.org/10.1175/JCLI-D-11-00230.1.

Pasquero, C., F. Desbiolles, and A. N. Meroni, 2021: Air-sea interactions in the cold wakes of tropical cyclones. *Geophys. Res. Lett.*, **48**, e2020GL091185, https://doi.org/10.1029/2020GL091185.

Renault, L., A. Hall, and J. C. McWilliams, 2016: Orographic shaping of us west coast wind profiles during the upwelling season. *Climate Dyn.*, **46**, 273–289, https://doi.org/10.1007/s00382-015-2583-4.

Samelson, R. M., E. D. Skyllingstad, D. B. Chelton, S. K. Esbensen, L. W. O'Neill, and N. Thum, 2006: On the coupling of wind stress and sea surface temperature. *J. Climate*, **19**, 1557–1566, https://doi.org/10.1175/JCLI3682.1.

Schneider, N., 2020: Scale and Rossby-number dependence of observed wind responses to ocean-mesoscale sea surface temperatures. *J. Atmos. Sci.*, **77**, 3171–3192, https://doi.org/10.1175/JAS-D-20-0154.1.

——, and B. Qiu, 2015: The atmospheric response to weak sea surface temperature fronts. *J. Atmos. Sci.*, **72**, 3356–3377, https://doi.org/10.1175/JAS-D-14-0212.1.

Skyllingstad, E. D., D. Vickers, L. Mahrt, and R. Samelson, 2007: Effects of mesoscale sea-surface temperature fronts on the marine atmospheric boundary layer. *Bound.-Layer Meteor.*, **123**, 219–237, https://doi.org/10.1007/s10546-006-9127-8.

——, S. P. de Szoeke, and L. W. O'Neill, 2019: Modeling the transient response of tropical convection to mesoscale SST variations. *J. Atmos. Sci.*, **76**, 1227–1244, https://doi.org/10.1175/JAS-D-18-0079.1.

Small, R. J., and Coauthors, 2008: Air-sea interaction over ocean fronts and eddies. *Dyn. Atmos. Oceans*, **45**, 274–319, https://doi.org/10.1016/j.dynatmoce.2008.01.001.

Smith, S. D., 1988: Coefficients for sea surface wind stress, heat flux, and wind profiles as a function of wind speed and temperature. *J. Geophys. Res.*, **93**, 15 467–15 472, https://doi.org/10.1029/JC093iC12p15467.

Smith, H. L., D. J. Matthews, G. I. Taylor, and L. Crawshay, 1914: *Ice Observation, Meteorology and Oceanography in the*

North Atlantic Ocean: Report on the Work Carried Out by the SS "Scotia," in 1913. HM Stationery Office, 141 pp.

Spall, M. A., 2007: Midlatitude wind stress–sea surface temperature coupling in the vicinity of oceanic fronts. *J. Climate*, **20**, 3785–3801, https://doi.org/10.1175/JCLI4234.1.

Sullivan, P. P., J. C. McWilliams, J. C. Weil, E. G. Patton, and H. J. S. Fernando, 2021: Marine boundary layers above heterogeneous SST: Alongfront winds. *J. Atmos. Sci.*, **78**, 3297–3315, https://doi.org/10.1175/JAS-D-21-0072.1.

Takatama, K., and N. Schneider, 2017: The role of back pressure in the atmospheric response to surface stress induced by the Kuroshio. *J. Atmos. Sci.*, **74**, 597–615, https://doi.org/10.1175/JAS-D-16-0149.1.

Wai, M. M.-K., and S. A. Stage, 1989: Dynamical analyses of marine atmospheric boundary layer structure near the Gulf Stream oceanic front. *Quart. J. Roy. Meteor. Soc.*, **115**, 29–44, https://doi.org/10.1002/qj.49711548503.

Wallace, J. M., T. P. Mitchell, and C. Deser, 1989: The influence of sea-surface temperature on surface wind in the eastern equatorial pacific: Seasonal and interannual variability. *J. Climate*, **2**, 1492–1499, https://doi.org/10.1175/1520-0442(1989)002<1492:TIOSST>2.0.CO;2.

Wenegrat, J. O., and R. S. Arthur, 2018: Response of the atmospheric boundary layer to submesoscale sea surface temperature fronts. *Geophys. Res. Lett.*, **45**, 13 505–13 512, https://doi.org/10.1029/2018GL081034.